ChemComm

# NiFe Nanoframes *via* a Unique Structural Formation Induced by a Sonochemical Etching



| | |
|---|---|
| Journal: | *ChemComm* |
| Manuscript ID | CC-COM-06-2022-003253.R1 |
| Article Type: | Communication |
| | |

COMMUNICATION

# Ni–Fe Nanoframes *via* a Unique Structural Formation Induced by Sonochemical Etching

Azhar Alowasheeir,[a] Hiroki Nara,[a]* Miharu Eguchi[a,b] and Yusuke Yamauchi[a,b]*

Received 00th January 20xx,
Accepted 00th January 20xx

DOI: 10.1039/x0xx00000x

**A uniform nanoframe structure derived from a Prussian blue analogue (PBA) with an internal cavity is successfully synthesized by sonochemical etching. The uniquely structured PBA nanoframes possess a three-dimensional open structure and high surface area, resulting in enhanced electrochemical properties for the oxygen evolution reaction as a model reaction.**

Morphological and structural control of nanocrystals has been the subject of intensive research because it enables tuning of their final properties, thus enhancing their applications in catalysis, electronics, photonics, sensing, and biomedical research.[1–3] Prussian blue (PB) and its analogues (PBAs) are a promising class of porous coordination polymers with numerous potential applications owing to their unique physical and chemical properties.[4,5] To date, several strategies have been developed for the preparation of bimetallic PBAs with adjustable architectures to offer a variety of compositions and morphologies under various synthetic conditions, including soft/hard templates,[4,6] chemical etching,[4,7] element replacement,[8] epitaxial growth,[9,10] and cation exchange[4,11]. Recently, intricate structures such as hollow nanocubes and nanoframes (NFs) composed of transition metals (*e.g.*, Ni, Fe, Co, Mn) have attracted great interest as promising materials for realizing new properties.[4,12,13] In our study, Ni–Fe PBA nanocubes (Ni–Fe NCs) are converted to Ni–Fe PBA nanoframes (Ni–Fe NFs) *via* a sonochemical etching process with hydrochloric acid solution. Benefiting from their unique structural merits including a three-dimensional (3D) open structure and high surface area, the resulting Ni–Fe NFs exhibit enhanced electrochemical properties. Because the performance of a material in target applications is strongly dependent on its structural features, achieving morphological and structural control over PB and PBAs has emerged as a research focus in recent years.

In the past decades, 3D open nanostructures with internal cavities (*e.g.*, NFs) have been extensively studied as promising candidates for energy storage and conversion applications, such as rechargeable batteries[5], supercapacitors, and water splitting[4,9], because their large surface area provides a high loading capacity for guest species/molecules and the extra internal cavity allows them to pass easily into the internal cavity.[9,14] In this regard, several attempts have been made to synthesize highly open frameworks by chemical etching with an acid solution, where the etching reaction begins at less stable areas (*e.g.*, those with high defect concentrations[4,15,16]) to trim the corners, edges, or faces.[4,17] Such etching can provide more active sites for catalysis to accelerate various reactions.[16,18,19] However, to the best of our knowledge, the simple synthesis without additives and heating of uniformly sized and well-defined NFs with internal cavities from PBAs has never been reported to date.

Herein, we present a facile synthetic protocol to fabricate unique PBA NFs by utilizing a controlled sonochemical etching reaction under sonication at room temperature. Several key parameters, *e.g.*, etching times and acid concentrations, were carefully investigated to optimize our protocol.

Ni–Fe NFs were synthesized by a sonochemical etching process. Briefly, Ni–Fe NCs were first prepared by a precipitation method, in which nickel chloride hexahydrate and trisodium citrate dihydrate were mixed thoroughly in water followed by the addition of aqueous sodium ferrocyanide solution and aging at room temperature overnight. After the reaction was complete, the products were collected and washed several times then dried at 25 °C in a vacuum oven for 24 h. The obtained powder was used as the starting material to synthesize Ni–Fe NFs *via* sonochemical etching in 0.4 M HCl solution at room temperature. The detailed procedures are described in the ESI.†

[a] *JST-ERATO Yamauchi Materials Space-Tectonics Project and International Center for Materials Nanoarchitectonics (MANA), National Institute for Materials Science (NIMS), 1-1 Namiki, Tsukuba, Ibaraki 305-0044, Japan. E-mail: NARA.Hiroki@nims.go.jp, YAMAUCHI.Yusuke@nims.go.jp*

[b] *School of Chemical Engineering and Australian Institute for Bioengineering and Nanotechnology (AIBN), The University of Queensland, Brisbane, Queensland 4072, Australia.*

† Electronic Supplementary Information (ESI) available: See DOI: 10.1039/x0xx00000x

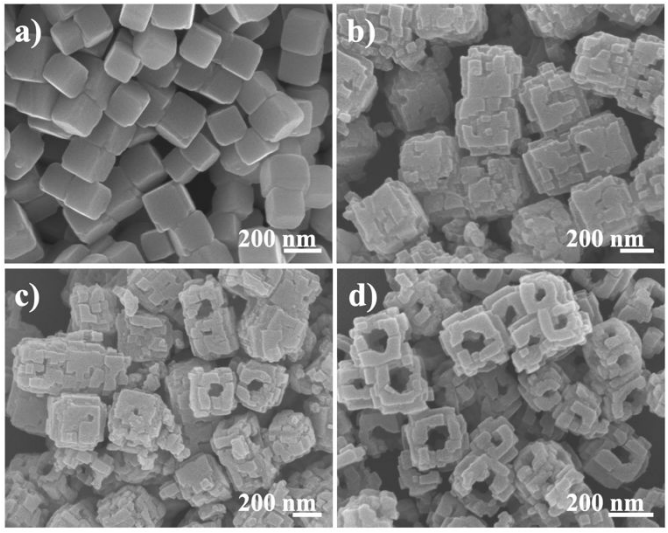


**Fig. 1** SEM images of (a) as-prepared Ni–Fe NCs and samples etched for (b) 10 min, (c) 20 min, and (d) 30 min.

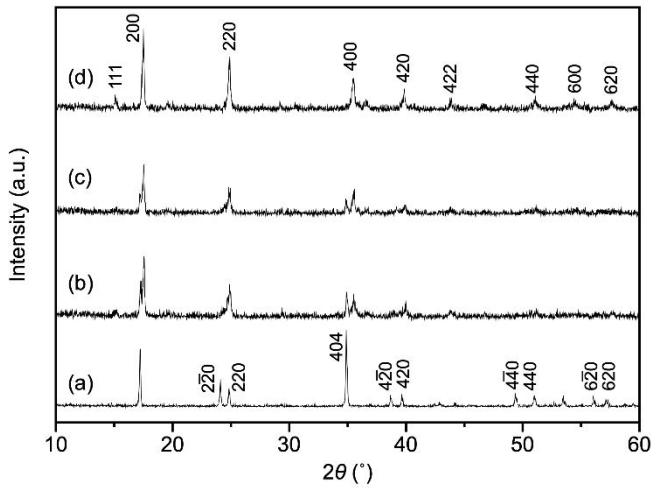


**Fig. 2** XRD patterns of (a) as-prepared Ni–Fe NCs and samples etched for (b) 10 min, (c) 20 min, and (d) 30 min.

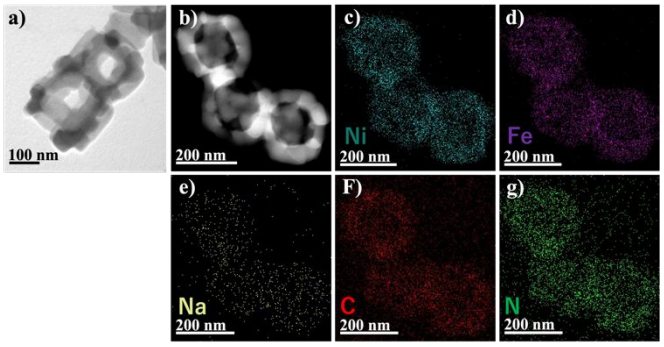


**Fig. 3** Microscopy images of NF-30: (a) TEM, (b) HAADF-STEM, and (c–g) elemental mapping for (c) nickel, (d) iron, (e) sodium, (f) carbon, and (g) nitrogen.

Scanning electron microscopy (SEM) and transmission electron microscopy (TEM) images clearly show that the starting Ni–Fe NCs possessed a homogeneous cubic architecture with a smooth surface and an average size of approximately 200 nm (**Fig. 1a** and **Fig. S1** in the ESI†). The wide-angle X-ray diffraction

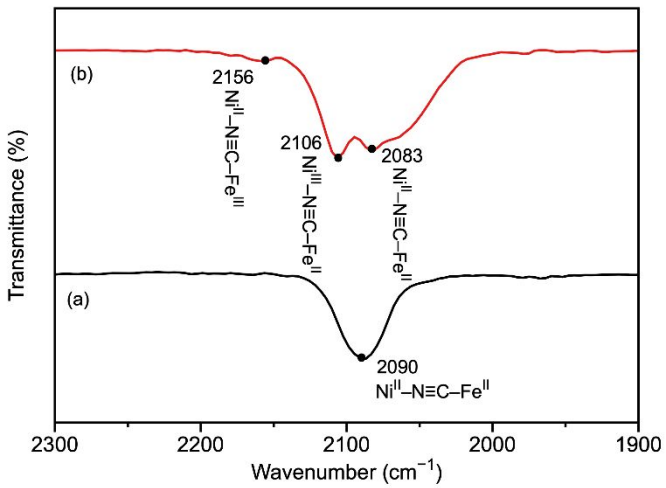


**Fig. 4** FTIR spectra of (a) the Ni–Fe NCs and (b) NF-30.

(XRD) pattern (**Fig. 2a**) contained sharp and intense diffraction peaks. The peaks corresponding to (220), (420), (440), and (620) were split with equal intensities, which indicates a high content of $Na^+$ ions in the interstitial sites.[20,21] The etching process was initiated by adding 0.4 M HCl solution to poweder of the Ni–Fe NCs (**Fig. 1b–d**). The use of sonication prevented severe aggregation of the particles during/after the chemical etching process (**Fig. S2**, ESI†).[22] The sample obtained after etching for 30 min, which is denoted NF-30 (NF-X, where X represents etching time), is shown in **Fig. 1d** and **3a**. The 3D open nanoframes can be clearly observed. The six faces of the Ni–Fe NCs were thus dissolved under the controlled conditions, leaving only the edges and corners remaining. The average particle size was not significantly altered compared with **Fig. 1a**.

Energy-dispersive X-ray spectra also confirmed that the elemental ratio of Ni:Fe was the same before and after sonochemical etching (1.0:0.9.). Nanoscale elemental mapping images revealed a uniform distribution of each element throughout the entire sample before and after etching (**Fig. 3** and **Fig. S1** in the ESI†). The obtained Ni–Fe NFs contained Ni, Fe, N, and C as the main elements, alongside a small amount of Na. It should be noted that the atomic ratio of $Na^+$ ions relative to Fe and Ni markedly decreased from 0.49 to 0.02 after etching (this is further discussed later).

The surface area of NF-30 was 451 $m^2\ g^{-1}$, considerably larger than that of the Ni–Fe NCs (47.8 $m^2\ g^{-1}$) (**Fig. S3**, ESI†). Time-dependent experiments were performed to investigate the structural transformation from NCs to NFs. As shown in **Fig. 1**, the structure and morphology of the intermediates after the various reaction stages were carefully examined by SEM. From **Fig. 1b** and **c**, it was confirmed that the edges of the cubes were etched first within 10 min, while after 20 min hollow cavities could be clearly observed on all of the faces. Upon extending the etching time to 1 h, most of the cubes disintegrated (**Fig. S4c**, ESI†). In the XRD patterns of samples for various etching

durations, the split peaks gradually converted to a single peak owing to the extraction of $Na^+$ from the lattice.[20,23]

The influence of the acid concentration was also investigated. After etching with 0.1 M HCl solution for 30 min (**Fig. S4a**, ESI†), the shape of the Ni–Fe NCs remained unaltered. By contrast, upon increasing the HCl concentration to 1.0 M, the sample surface became irregular (**Fig. S4b**, ESI†). However, the XRD patterns of the Ni–Fe NCs etched with 0.1 or 1.0 M HCl solution for 30 min were similar to those of NF-10, NF-20, and NF-30 (**Fig. 2b–d** and **Fig. S5** in the ESI†).

The Fourier-transform infrared (FTIR) spectrum of the starting Ni–Fe NCs (**Fig. 4** and **Fig. S6** in the ESI†) contained a single strong peak at 2090 $cm^{-1}$ corresponding to the stretching vibration of the cyano group in $Ni^{II} - N \equiv C - Fe^{II}$.[24–26] After initiation of the etching reaction, this characteristic stretching vibration of the CN group was observed in two or more locations irrespective of the etching duration. The NF-10, NF-20, and NF-30 samples exhibited the $Ni^{II}$–$N \equiv C$–$Fe^{II}$ peaks at 2100, 2094, and 2083 $cm^{-1}$ alongside $Ni^{II}$–$N \equiv C$–$Fe^{III}$ peaks at 2167, 2165, and 2156 $cm^{-1}$, respectively.[26,27] Another peak at 2106 $cm^{-1}$ in the NF-30 sample was ascribed to $Ni^{III}$–$N \equiv C$–$Fe^{II}$.[28,29] These FTIR results confirm the coexistence of two Fe valence states after HCl addition irrespective of the etching duration, indicating the transformation of $Ni^{II}$ and $Fe^{II}$ due to proton-coupled electron transfer.[30] In general, the $Ni^{II}$–$N \equiv C$–$Fe^{III}$ moieties are primarily located at the nanocube center (core), whereas the $Ni^{II}$–$N \equiv C$–$Fe^{II}$ moieties lie near the surface.[15] The chemical bonding between $Ni^{II}$ and $-N \equiv C$–$Fe^{II}$ (near the surface) is stronger than that between $Ni^{II}$ and $-N \equiv C$–$Fe^{III}$ (at the core) owing to the strong electron-donating ability of the N atom in $-N \equiv C$–$Fe^{II}$, which makes the bond in $Ni^{II}$–$N \equiv C$–$Fe^{III}$ weaker and more easily broken.[4,26] Thus, the HCl can preferentially cleave these weak bonds in the center of the nanocube surface to form the unique hollow interior. In addition, the sample color changed from light green to cyan and finally blue with increasing etching time (**Fig. S6**, ESI†).

The oxygen evolution reaction (OER) is an important anodic half-reaction in electrochemical energy technologies.[31] **Fig. 5** presents the cyclic voltammograms of the Ni–Fe NCs and NF-30 recorded in the anodic direction at a scan rate of 10 mV $s^{-1}$ in 0.1 M KOH solution. According to the dashed lines extrapolatedfrom the curves between 1.6 and 1.7 V *vs*. RHE, the onset potential was estimated to be 1.52 V *vs*. RHE for both samples, indicating that the nanoframe structure did not affect the overpotential of the NF-based catalyst.On the other hand,

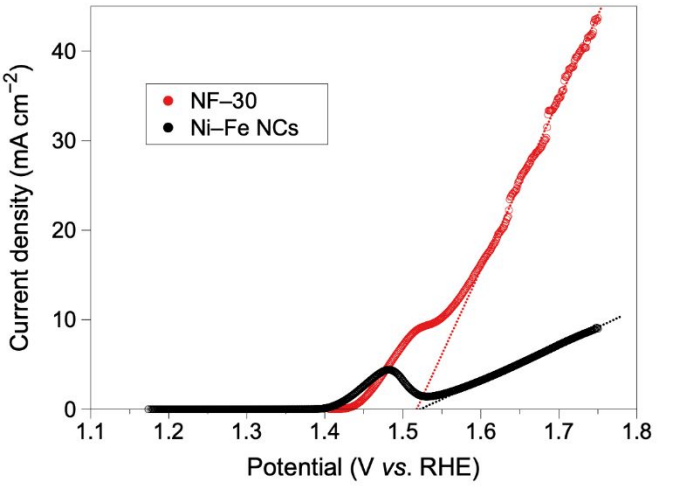


**Fig. 5** Anodic cyclic voltammograms (*iR*-corrected) for the Ni–Fe NCs and NF-30 recorded at a scan rate of 10 mV $s^{-1}$ in 0.1 M KOH solution. The potential was converted from the potential of Hg/HgO (1 M NaOH) (905 mV *vs*. RHE).

the nanoframe structure effectively improved the OER current density, which reached 43.7 mA $cm^{-2}$ at 1.75 V *vs*. RHE, 4.9 times higher than that for the Ni–Fe NCs. To compare the effect of the electrochemically active surface area, the double-layer capacitance was calculated from cyclic voltammograms measured around the open circuit potential at various scan rates (**Fig. S7**, ESI†), affording values of 0.073 and 0.257 F $g^{-1}$ for the Ni–Fe NCs and NF-30, respectively. These results indicate that the electrochemically active surface area was 3.5 times higher for NF-30 than for the Ni–Fe NCs. In addition, the currents normalized with respect to the double-layer capacitance were compared (**Fig. S8**, ESI†), further demonstrating the effectiveness of the nanoframe structure. Prior to the OER, an obvious anodic peak at 1.48 V *vs*. RHE was observed. This was ascribed to a reversible redox reaction involving a valence change of Ni (**Fig. S9a**, ESI†).[32] This was confirmed by the cyclic voltammograms. When the anodic scan direction was reversed at an initial rise of the anodic current, the cathodic current was not observed (**Fig. S9b** and **d**, ESI†). Also, when the cathodice scan direction was reversed at an initial rise of the cathodic current, the anodic current was not observed (**Fig. S9c** and **e**, ESI†).

The electrode stability was evaluated by chronoamperometry at 1.66 V *vs*. RHE under severe conditions where $O_2$ bubbles were vigorously formed (**Fig. S10**, ESI†). Both the Ni–Fe NCs and NF-30 were unstable under these conditions. After 15 h, most of the catalyst had physically peeled off from the rotating disk electrode owing to the stress caused by the severe bubble generation. It should be noted that the decrease rate of the current density differed for the two samples, with NF-30 displaying a lower decrease rate than the Ni–Fe NCs. This is probably attributable to the nanoframe structure, where the higher surface area and superior mass transport reduced the local frequency of bubble generation and concomitant stress. Thus, the creation of the hollow nanoframe structure was found to be effective for improving the OER catalytic activity.

In summary, we have successfully prepared Ni–Fe NFs with a high surface area by subjecting Ni–Fe NCs to sonochemical

etching at room temperature. Time-dependent observations clearly revealed the morphological evolution mechanism from nanocubes to nanoframes. The obtained nanoarchitectures represent potential electrode materials for future energy conversion and storage systems.

This work was supported by JST ERATO Grant Number JPMJER2003, Japan.

## Author Contributions

Azhar Alowasheeir: Investigation, Visualization, Writing – original draft. Hiroki Nara: Investigation, Visualization, Writing – original draft, Writing – review & editing. Miharu Eguchi: Supervision, Writing – review & editing. Yusuke Yamauchi: Conceptualization, Supervision, Funding acquisition, Project administration, Writing – review & editing.

## Conflicts of interest

There are no conflicts to declare

## Notes and references

1 A. Azhar, Y. Li, Z. Cai, M. B. Zakaria, M. K. Masud, M. S. A. Hossain, J. Kim, W. Zhang, J. Na, Y. Yamauchi and M. Hu, *Bull. Chem. Soc. Jpn.*, 2019, **92**, 875–904.
2 X. Zhang, J. Tang, N. Zhu, L. Li and Y. Wang, *Environ. Chem. Lett.*, 2022, **20**, 1035–1045.
3 H. Kim, T. Y. Yoo, M. S. Bootharaju, J. H. Kim, D. Y. Chung and T. Hyeon, *Adv. Sci.*, 2022, **9**, 2104054.
4 J. Nai, X. Wen, D. Lou, J. W. Nai and X. W. Lou, *Adv. Mater.*, 2019, **31**, 1706825.
5 B. Wang, Y. Han, X. Wang, N. Bahlawane, H. Pan, M. Yan and Y. Jiang, *iScience*, 2018, **3**, 110–133.
6 A. Azhar, M. B. Zakaria, E. Z. M. Ebeid, T. Chikyow, Y. Bando, A. A. Alshehri, Y. G. Alghamdi, Z. X. Cai, N. A. Kumar, J. Lin, H. Kim and Y. Yamauchi, *ChemistryOpen*, 2018, **7**, 599–603.
7 L. M. Cao, D. Lu, D. C. Zhong and T. B. Lu, *Coord. Chem. Rev.*, 2020, **407**, 213156.
8 J. G. Wang, Z. Zhang, X. Zhang, X. Yin, X. Li, X. Liu, F. Kang and B. Wei, *Nano Energy*, 2017, **39**, 647–653.
9 L. Yu, H. bin Wu and X. W. D. Lou, *Acc. Chem. Res.*, 2017, **50**, 293–301.
10 J. Nai, J. Zhang and X. W. (David) Lou, *Chem*, 2018, **4**, 1967–1982.
11 W. Zhang, H. Song, Y. Cheng, C. Liu, C. Wang, M. A. N. Khan, H. Zhang, J. Liu, C. Yu, L. Wang and J. Li, *Adv. Sci.*, 2019, **6**, 1801901.
12 A. Reddy Mule, B. Ramulu, J. Su Yu, A. R. Mule, B. Ramulu and J. S. Yu, *Small*, 2022, **18**, 2105185.
13 V.-T. Hoang, N. le Nhat Trang, D. Thi Nguyet Nga, al -, W. Li, Y. Liu, Y. Guo -, S. Tamiya, T. Sato, M. Kushida -, Y. Wang, D. Su, A. Ung, J. Ahn and G. Wang, *Nanotechnology*, 2012, **23**, 055402.
14 Y. Shan, G. Zhang, W. Yin, H. Pang and Q. Xu, *Bull. Chem. Soc. Jpn.*, 2021, **95**, 230–260.
15 H. Zhang, Q. Jiang, J. H. L Hadden, F. Xie, D. Jason Riley, H. Zhang, Q. Jiang, J. H. L Hadden, F. Xie and D. J. Riley, *Adv. Funct. Mater.*, 2021, **31**, 2008989.
16 Y. Zhu, B. Wang, Q. Gan, Y. Wang, Z. Wang, J. Xie, S. Gu, Z. Li, Y. Li, Z. W. Ji, H. Cheng and Z. Lu, *Inorg. Chem. Front.*, 2019, **6**, 1361–1366.
17 L. Catala and T. Mallah, *Coord Chem Rev*, 2017, **346**, 32–61.
18 W. Zhang, Y. Zhao, V. Malgras, Q. Ji, D. Jiang, R. Qi, K. Ariga, Y. Yamauchi, J. Liu, J. sen Jiang and M. Hu, *Angew. Chem. Int. Ed.*, 2016, **55**, 8228–8234.
19 W. Ren, M. Qin, Z. Zhu, M. Yan, Q. Li, L. Zhang, D. Liu and L. Mai, *Nano Lett.*, 2017, **17**, 4713–4718.
20 X. Wu, C. Wu, C. Wei, L. Hu, J. Qian, Y. Cao, X. Ai, J. Wang and H. Yang, *ACS Appl. Mater. Interfaces*, 2016, **8**, 5393–5399.
21 X. H. Ma, Y. Y. Wei, Y. D. Wu, J. Wang, W. Jia, J. H. Zhou, Z. F. Zi and J. M. Dai, *Electrochim. Acta*, 2019, **297**, 392–397.
22 S. T. Aruna, C. Anandan and V. K. W. Grips, *Appl. Surf. Sci.*, 2014, **301**, 383–390.
23 Y. Tang, W. Zhang, L. Xue, X. Ding, T. Wang, X. Liu, J. Liu, X. Li and Y. Huang, *J. Mater. Chem. A*, 2016, **4**, 6036–6041.
24 H. Sun, W. Zhang and M. Hu, *Crystals 2018, Vol. 8, Page 23*, 2018, **8**, 23.
25 L. L. Wu, X. H. Chen, Q. Zhang, J. Luo, H. C. Fu, L. Shen, H. Q. Luo and N. B. Li, *Appl. Surf. Sci.*, 2021, **567**, 150835.
26 J. Nai, Y. Lu, L. Yu, X. Wang, X. Wen, D. Lou, J. W. Nai, Y. Lu, L. Yu, X. Wang and X. W. Lou, *Adv. Mater.*, 2017, **29**, 1703870.
27 Q. Niu, C. Bao, X. Cao, C. Liu, H. Wang and W. Lu, *Biosens. Bioelectron.*, 2019, **141**, 111445.
28 S. J. Gerber and E. Erasmus, *Mater. Chem. Phys.*, 2018, **203**, 73–81.
29 Y. Feng, X. Wang, P. Dong, J. Li, L. Feng, J. Huang, L. Cao, L. Feng, K. Kajiyoshi and C. Wang, *Sci. Rep.*, 2019, **9**, 1–11.
30 J. Nai, B. Y. Guan, L. Yu and X. Wen David Lou, *Sci. Adv.*, 2017, **3**, e1700732.
31 M. Yu, E. Budiyanto and H. Tüysüz, *Angew. Chem. Int. Ed.*, 2022, **61**, e202103824.
32 L. Trotochaud, S. L. Young, J. K. Ranney and S. W. Boettcher, *J. Am. Chem. Soc.*, 2014, **136**, 6744–6753.